How to Cite: Mulyukina, S.M., Dzeranov, A.A., Pankratov, D.A., Bondarenko, L.S., Kugabaeva, G.D., Prokofiev, M.V., & Kydralieva, K.A. (2026). Engineering Biocompatible Goethite Nanoparticles: Microstructural Tuning through Controlled Ferrihydrite Conversion Routes. *Eurasian Journal of Chemistry, 31, 1(121), 121–136.* https://doi.org/10.31489/2959-0663/1-26-9

Article

Received: 2 December 2025 | Revised: 2 February 2026 |
Accepted: 12 February 2026 | Published online: 19 February 2026

UDC 544.42+519.242.7

https://doi.org/10.31489/2959-0663/1-26-9

Sofia M. Mulyukina[1]*, Artur A. Dzeranov[2, 3], Denis A. Pankratov[4, 5],
Lyubov S. Bondarenko[2], Gulsara D. Kugabaeva[2, 3], Mikhail V. Prokofiev[2],
Kamila A. Kydralieva[2]

[1]*Surgut State University, Surgut, Russia;*
[2]*Moscow Aviation Institute (National Research University), Moscow, Russia;*
[3]*Federal Research Center of Problems of Chemical Physics and Medicinal Chemistry,*
Russian Academy of Sciences, Moscow Region, Russia;
[4]*Lomonosov Moscow State University, Moscow, Russia;*
[5]*Moscow Institute of Physics and Technology (National Research University), Moscow region, Russia*
*(*Corresponding author's e-mail: sbolotskaya@inbox.ru)*

Engineering Biocompatible Goethite Nanoparticles: Microstructural Tuning through Controlled Ferrihydrite Conversion Routes

The goethite (α-FeOOH) nanoparticles (NPs) are highly attractive material with a broad spectrum of applications, including biomedicine thanks to a high thermodynamical stability. The formation and strict control of the phase-pure goethite NPs remain a challenging task due to the high sensitivity of the particles to the synthesis conditions. This study presents for the first time effect of the iron source (nitrate vs. chloride) and alkaline medium (NaOH vs. NH_4OH) on three known distinct post-synthesis transformation pathways for preparing goethite NPs from ferrihydrite suspensions: aging, ultrasonic-assisted conversion, and hydrothermal crystallization. We observed that ferrihydrite NPs precursor generated from $FeCl_3$ with NaOH facilitated the formation of phase-pure goethite through both aging and ultrasonic transformation under ambient conditions. In contrast, synthesis at 90 °C promoted the formation of larger crystals, often accompanied by significant phase impurities. For the first time, comprehensive characterization of the synthesized materials was performed in addition to previously used methods as X-ray diffraction, the ^{57}Fe Mössbauer spectroscopy, transmission electronic microscopy, and low-temperature nitrogen adsorption/desorption enabling in-depth assessment of crystallinity, phase purity, and morphological features. These findings highlight the potential of iron-based goethite nanomaterials as safe, functional, and versatile platforms for future biomedical and technological applications.

Keywords: goethite nanoparticles, ferrihydrite precursor, aging, ultrasonic-assisted conversion, hydrothermal crystallization, post-synthesis transformation, iron source, alkaline medium, crystal structure

Introduction

Goethite (α-FeOOH) is one of the most thermodynamically stable and environmentally ubiquitous iron oxyhydroxides, commonly occurring in solis, sediments, and aqueous systems. Owing to its chemical robustness, non-toxicity, low cost, and the abundance of reactive hydroxyl groups on its surface, goethite is a highly attractive material with a broad spectrum of applications [1]. These include bioinspired and biomimetic scaffolds for biomedical use [2–4]. For example, a recent study [2] employed spongin extracted from the marine demosponge *Hippospongia communis* as a microporous template for constructing a 3D goethite-based composite with enhanced electrochemical performance for dopamine sensing in human urine. Nano-sized goethite exhibits significant antibacterial properties against *E. coli* O157:H7 by damaging bacterial membranes, mediated by both ROS-dependent RNA damage and cell membrane destruction [5]. The exposure to nano-sized goethite increased the levels of ribonucleoside-related substances, phenylalanine and adenosine 5′-triphosphate, while decreased those of glycogen, protein and lipopolysaccharide & outer membrane porins (LPS & OMPs). Goethite shows promising anti-parasitic effects, particularly against the protozoan Toxoplasma gondii, with studies revealing that goethite nanoparticles can significantly reduce parasite viability, potentially offering new therapeutic avenues, especially when combined with surface modifications like L-tryptophan for improved targeted toxicity, addressing the need for better treatments for diseases like toxoplasmosis [6]. Furthermore, α-FeOOH has emerged as a promising functional material in photocatalytic systems [6–10], for oxidation of other toxicants [11].

Numerous synthetic strategies have been developed for the preparation of α-FeOOH nanoparticles (NPs), including Fe(III) coprecipitation [1, 12, 13], rapid ferrihydrite transformation via ultrasonic irradiation, sol–gel methods, and microemulsion techniques [14, 15]. However, the synthesis and structural control of iron (oxyhydr)oxides remains a significant challenge since there is no single synthesis protocol. Varying the conditions of NPs synthesis in order to find scientifically sound methods is associated with the impossibility of achieving the formation of monophasic NPs with specified properties for various potential target applications within the framework of the same synthesis conditions. The hydrolysis of Fe^{2+} and Fe^{3+} in aqueous systems can yield a complex mixture of hydroxides, oxyhydroxides, and oxides, as their formation is highly sensitive to parameters such as pH, ionic strength, temperature, and precursor identity [16]. Thus, precise control over synthesis conditions is critical to direct the formation of a desired phase. Synthesis approaches often used lead to the production of a mixture of several phases rather than a monophase product. So obtaining goethite by the hydrothermal method, declare a mixture of phases of 70, 21.6 magnetite and 8.4 % hematite [17]. The authors [18] using wet synthesis approaches, according to X-ray phase analysis data, a mixture is obtained Hematite 47(3) %; Goethite 19(2) %; Magnetite 1.7(13) %; Quartz 6(2) %. Interestingly, the authors [19], obtaining goethite by co-precipitation with further aging overnight at 14 °C, declare the preservation of the goethite phase in the XRD analysis and the appearance of the hematite phase in the analysis by Mossbauer spectroscopy.

The morphological and structural properties of goethite are highly dependent on the chosen synthetic pathway [1, 16, 20, 21]. For instance, Kosmulski et al. [19] demonstrated that parameters such as the Fe(III) : OH^- ratio, titration rate, and crystallization temperature and duration markedly influence the specific surface area and overall particle characteristics. Similarly, Meret et. al. [22] showed that the low-temperature transformation of ferrihydrite into goethite proceeds slowly under mild conditions, and its final phase composition is sensitive to both pH and thermal input. Ristic et al. [23] demonstrated that variations in parameters such as pH, weight of the initial precursor sample, temperature, and retention time during co-precipitation in a highly alkaline medium led, for example, to partial conversion of goethite to hematite. In the study Xu et al. [24], E. coli adapted to goethite at a concentration of 1 mg/mL did not acquire antibiotic resistance even after 13 generations, probably due to its poor biofilm-formation capacity. In the article Agresti [25], the electrorheological properties of suspensions of lamellar goethite (α-FeOOH) nanoparticles in silicone oil are investigated. The particles were synthesized and functionalized with urea to increase polarizability. Electrorheological characterization has shown that urea functionalization enhances rheological properties (limiting shear stress and viscosity) under the action of an electric field up to 5 kV/mm, which allows achieving similar characteristics at a lower filler concentration. The results demonstrate the potential of functionalized goethite as an efficient and economical material for smart electrorheological fluids. Darabian et al. [26] showed that low oxygen flow rates (0.025, 0.017, 0.013, 0.01 cm^3/s) during the oxidation of $Fe(OH)_2$ to obtain goethite led to the secondary production of magnetite and maghemite, registered by the XRD. In general, varying the oxygen flow rate led to a change in particle size and specific surface area. Other studies using hydrothermal methods revealed that the choice of iron precursor has a pronounced impact on phase evolution: ferric nitrate tends to favor goethite formation, while ferric chloride and ferric sulfate may result in akaganéite, lepidocrocite, or mixed-phase nanocomposites such as goethite/parabutlerite [27–29]. Goethite NPs could be used as T_2 MRI contrasting agents with unique properties which are not suffering from upper size limitations [30–33].

In this study, we systematically investigated the hydrolysis of Fe(III) at pH 12 to selectively promote the formation of monophasic goethite, following the thermodynamic framework proposed by Cudennec and Lecerf [16].

The aim of this study was to determine synthesis conditions that would yield goethite nanoparticles while avoiding secondary phases that could affect reactivity, using a wider range of methods, including Mössbauer spectroscopy, a more powerful technique than X-ray diffraction. To achieve this, we employed a comparative analysis of several known distinct synthesis routes: ferrihydrite aging, ultrasonic-assisted conversion, and hydrothermal crystallization by variation for the first time key parameters within these routes, including the iron source (nitrate vs. chloride), alkaline medium (NaOH vs. NH_4OH). The resulting nanostructures were comprehensively characterized in addition to previously used methods as X-ray diffraction, the ^{57}Fe Mössbauer spectroscopy, transmission electronic microscopy, and low-temperature nitrogen adsorption/desorption enabling us to correlate synthesis conditions (iron source and alkaline medium) with the phase composition, morphology, and textural properties of the goethite NPs prepared.

Experimental

Materials

In this work, the following reagents were used: iron(III) nitrate nonahydrate $Fe(NO_3)_3{\cdot}9H_2O$ (extra pure grade; Prime Chemicals Group, Russia); iron(III) chloride hexahydrate $FeCl_3{\cdot}6H_2O$ (extra pure grade; Krasnaya Zvezda Trading House, Russia); sodium hydroxide NaOH (analytical grade; Reachim, Russia); and ammonium hydroxide solution 25 % NH_4OH (extra pure grade; SigmaTek, Russia).

All the dry substances used were previously dissolved in deionized water with a certain molarity for subsequent syntheses.

Synthesis of Goethite NPs

Goethite (α-FeOOH) NPs were synthesized using three distinct approaches for the conversion of ferrihydrite suspensions: 1) Aging of ferrihydrite suspensions obtained by coprecipitation (Samples A-N and A-C); 2) Rapid transformation of ferrihydrite via ultrasonic irradiation (Samples U-N and U-C) [1]; 3) Hydrothermal treatment (Samples H-N and H-C) [34]. In all procedures, the pH was adjusted and maintained during all process at approximately 12 to ensure the dominance of hydroxo ions, which are essential for goethite formation. The iron precursors used were iron(III) nitrate ($Fe(NO_3)_3{\cdot}9H_2O$) and iron(III) chloride ($FeCl_3{\cdot}6H_2O$) [1], with specific precursors corresponding to different samples (e.g., Sample A-N used iron(III) nitrate, while Sample A-C used iron(III) chloride, and similar variations applied to other sample pairs).

Method 1.1 — Aging (Iron(III) Nitrate)

Goethite nanoparticles were prepared by the dropwise addition of 45 mL of 1.5 M NaOH to 5 mL of 0.06 M $Fe(NO_3)_3{\cdot}9H_2O$ at room temperature under constant stirring (100 rpm), while maintaining the pH at 12 during all process. The resulting ferrihydrite suspension was aged for 3 days at ambient conditions. The precipitate was then washed with deionized water until it reached a neutral pH, centrifuged (10 min, 3000 rpm), and dried in a desiccator at 60 °C for 24 hours. The final yield was 0.64 g.

Method 1.2 — Aging (Iron(III) Chloride)

This sample was synthesized following the same protocol as Method 1.1, but with $FeCl_3{\cdot}6H_2O$ used as the iron source. The yield was 0.75 g.

Method 2.1 — Ultrasonic Conversion (Iron(III) Nitrate)

A 5.625 M NaOH solution was added to 20 mL of 0.1 M $Fe(NO_3)_3{\cdot}9H_2O$ under continuous stirring (100 rpm) until the pH reached 12. The mixture was then subjected to ultrasonic treatment (30 kHz, 60 W, ultrasound bath, complete immersion of sample in a test tube in water) for 1 hour at 30 °C, pH was maintained during all process. The precipitate was washed with deionized water to neutral pH, centrifuged (10 min, 3000 rpm), and dried in a desiccator at 60 °C for 10 hours. The yield was 0.93 g.

Method 2.2 — Ultrasonic Conversion (Iron(III) Chloride)

This sample followed the same procedure as Method 2.1, using $FeCl_3{\cdot}6H_2O$ as the iron precursor. The final yield was 0.297 g.

Method 3.1 — Hydrothermal (Iron(III) Nitrate)

A total of 47 mL of 0.33 M $Fe(NO_3)_3{\cdot}9H_2O$ was mixed with 80 mL of 25 % NH_4OH, and the pH was adjusted to 12. The reaction mixture was heated at 90 °C for 2 hours without allowing vigorous boiling, pH was maintained during all process, then cooled to room temperature and left undisturbed for 24 hours. The solid was washed with deionized water until pH 6, centrifuged (15 min, 6000 rpm), and dried in a desiccator at 60 °C for 24 hours. The yield was 2.23 g.

Method 3.2 — Hydrothermal (Iron(III) Chloride)

This sample was synthesized using the same procedure as Method 3.1, replacing the nitrate salt with $FeCl_3{\cdot}6H_2O$. The yield was 2.95 g.

Table 1

Designations of samples and corresponding synthesis parameters

Method	Type of iron precursor	
	Cl^-	NO_3^-
Aging	A-C	A-N
Ultrasonic Conversion	U-C	U-N
Hydrothermal	H-C	H-N

Characteristics of Samples

X-ray Diffraction (XRD)

The crystal structure and phase composition of the synthesized NPs were analyzed by X-ray diffraction (XRD) using a Thermo Fisher Scientific ARL X'TRA diffractometer equipped with $Cu_{K\alpha}$ radiation (λ=1.54184 Å). Measurements were conducted over a 2θ range of 10–95° at a scanning speed of 5 deg/min and a temperature of 25 °C. The full width at half maximum (FWHM) was used for particle size determination with the Scherrer equation [29]. The diffraction patterns were processed using the Rietveld method in the Match! software. The final diffraction patterns were constructed in OriginPro software.

Mössbauer Spectroscopy

^{57}Fe Mössbauer absorption spectra (MS) were recorded in transmission geometry with a moving source and triangular velocity reference signal using an MS1104EM Mössbauer spectrometer (CJSC Kordon, Rostov-on-Don, Russia). Measurements were performed at 296(3) K and 77.7(3) K using a cryogen-free closed-cycle cryostat (CFPR-221-MESS). The γ-radiation source consisted of ^{57}Co in a metallic rhodium matrix (10 mCi activity; Cyclotron Co., Ltd, Obninsk, Russia) and was maintained at room temperature. An α-Fe foil was used as a reference absorber for velocity calibration. The signal-to-noise ratio did not exceed 2 %. High-resolution spectra (1024 channels) were processed using the SpectRelax 3.4 software package (Lomonosov Moscow State University, Russia). Isomer shifts are reported relative to α-Fe at 296 K.

Transmission Electron Microscopy (TEM)

The morphology of the NPs was examined using transmission electron microscopy (TEM). Prior to imaging, samples were dispersed in deionized water and sonicated with an ultrasonic processor (Fisherbrand, USA) at 75 % amplitude to promote homogenization and prevent aggregation. A 10 μL droplet of the suspension was deposited onto a 200-mesh carbon-coated copper grid (Ted Pella Inc., USA), which had been pretreated via glow discharge (PELCO Inc., USA) to enhance particle adhesion. After 1 minute of incubation at room temperature, excess liquid was blotted off with filter paper. The grids were mounted on the TEM stage, and imaging was performed using a Tecnai G2-20 transmission electron microscope (FEI Company, Hillsboro, OR, USA) operated at 120 kV. Particle size distributions were determined by analyzing at least 100 particles per image using ImageJ software (National Institutes of Health, USA).

Specific Surface Area and Porosity Analysis (BET/BJH)

The specific surface area (SSA) and porous structure characteristics of the samples were evaluated using a Sorbtometer-M instrument (Katakon, Russia). Measurements relied on nitrogen adsorption-desorption isotherms obtained at liquid nitrogen temperature (77 K). During testing, a stationary flow of a helium–nitrogen gas mixture (with the nitrogen volume fraction ranging from 0 to ≈1) was passed over the sample. Desorption isotherms were constructed by measuring the volume of nitrogen released upon heating (approximately −100 °C), while adsorption isotherms were obtained as the nitrogen volume fraction decreased from ≈1 to 0. SSA and pore structure parameters were calculated using the Brunauer–Emmett–Teller (BET) method and the Barrett–Joyner–Halenda (BJH) method, respectively. Prior to analysis, all samples underwent degassing ("thermoregulation") at 150 °C under vacuum in a stationary nitrogen flow to remove adsorbed gases and vapors.

Results and Discussion

Phase Composition (XRD)

The crystalline structure and phase composition of the synthesized NPs were comprehensively evaluated via X-ray diffraction (XRD). Representative diffractograms for all samples are presented in Figure 1. XRD analysis revealed that the final phase composition was highly sensitive to synthesis parameters, including the identity of the iron precursor, the nature of the alkaline medium, and the applied thermal conditions [35-36]. Samples A-C and U-C were found to consist predominantly of goethite (α-FeOOH) [37], demonstrating that these specific synthesis routes effectively favored the crystallization of a monophasic product. In contrast, alternative conditions yielded more complex or multiphase systems. Sample A-N yielded primarily goethite with a minor secondary phase. This secondary component was identified by Mössbauer spectroscopy as a paramagnetic Fe^{3+} octahedral species (Fe^{3+}_{Oh}), typical of superparamagnetic iron oxyhydroxides.

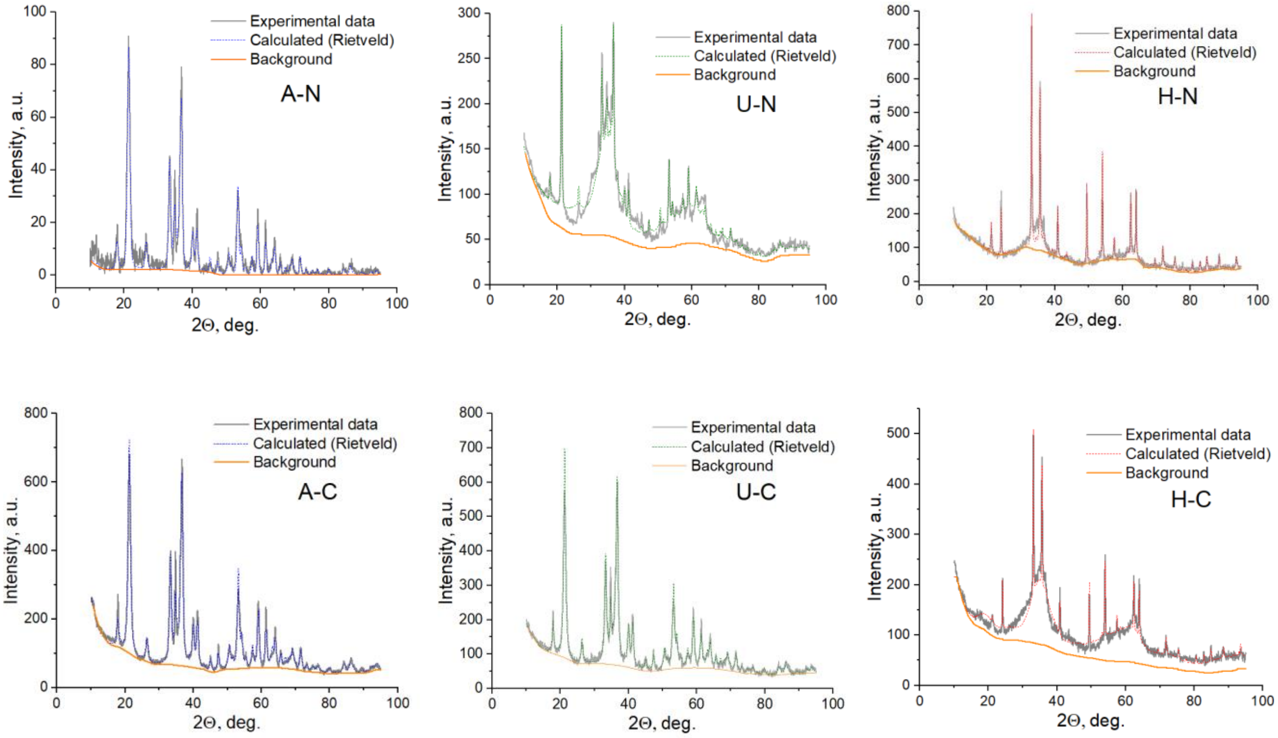

Figure 1. X-ray diffraction of synthesized iron (oxyhydr)oxide NPs

Sample U-N was dominated by ferrihydrite ($5Fe_2O_3·9H_2O$), [38, 39] a poorly crystalline iron oxyhydroxide, as evidenced by its broad diffraction hump centered near 62° 2θ (Fig. 1), a hallmark of bilayer-type ferrihydrite [40]. Sample H-N displayed a well-defined crystalline pattern characteristic of hematite (α-Fe_2O_3), as indicated by sharp peaks near 32° 2θ (Fig. 1) [17]. Although minor goethite reflections were also detected around 20° 2θ, these were less pronounced, suggesting it formed as a secondary product under hydrothermal conditions [41]. Sample H-C exhibited the most complex phase composition. Its diffractogram revealed a mixture of ferrihydrite, hematite, and goethite, with the latter present only in minor quantities (Fig. 1). Collectively, these findings emphasize the pivotal role of synthesis design, particularly the iron salt identity, base selection, and thermal regime, in governing the crystallization and final properties of iron oxyhydroxide NPs.

Table 2

X-ray diffraction data for synthesized goethite NPs

Sample	*a*, Å	*b*, Å	*c*, Å	$(GoF)^2$	Composition	Amount, %	*D*, nm	No COD
A-N	4.607	9.945	3.019	1.2	α-FeOOH	79	13±4	9003078
A-C	4.616	9.945	3.021	0.8	α-FeOOH	96	15±5	1008768
U-N	6.175	–	9.205	0.9	$5Fe_2O_3 \cdot 9H_2O$	79	28±2	2211652
	4.606	9.971	3.023		α-FeOOH	20		9011571
U-C	4.617	9.996	3.024	0.9	α-FeOOH	96	18±6	9002158
H-N	5.037	–	13.765	1.1	α-Fe_2O_3	76	31±5	9000139
	4.671	9.392	3.028		α-FeOOH	18		9003079
H-C	6.118	–	9.062	0.9	$5Fe_2O_3 \cdot 9H_2O$	84	41±10	9011573
	5.038	–	13.778		α-Fe_2O_3	14		9000139
	4.603	10.098	3.022		α-FeOOH	1		9003077

Note: *GoF — goodness of fit, COD — Crystallography Open Database.

Phase Composition and Magnetic Properties (Mössbauer Spectroscopy)

To complement the crystallographic insights provided by XRD, detailed phase composition and magnetic behavior of the synthesized iron (oxyhydr)oxide NPs were examined using ^{57}Fe Mössbauer spectroscopy. Representative spectra for all samples are presented in Figure 2.

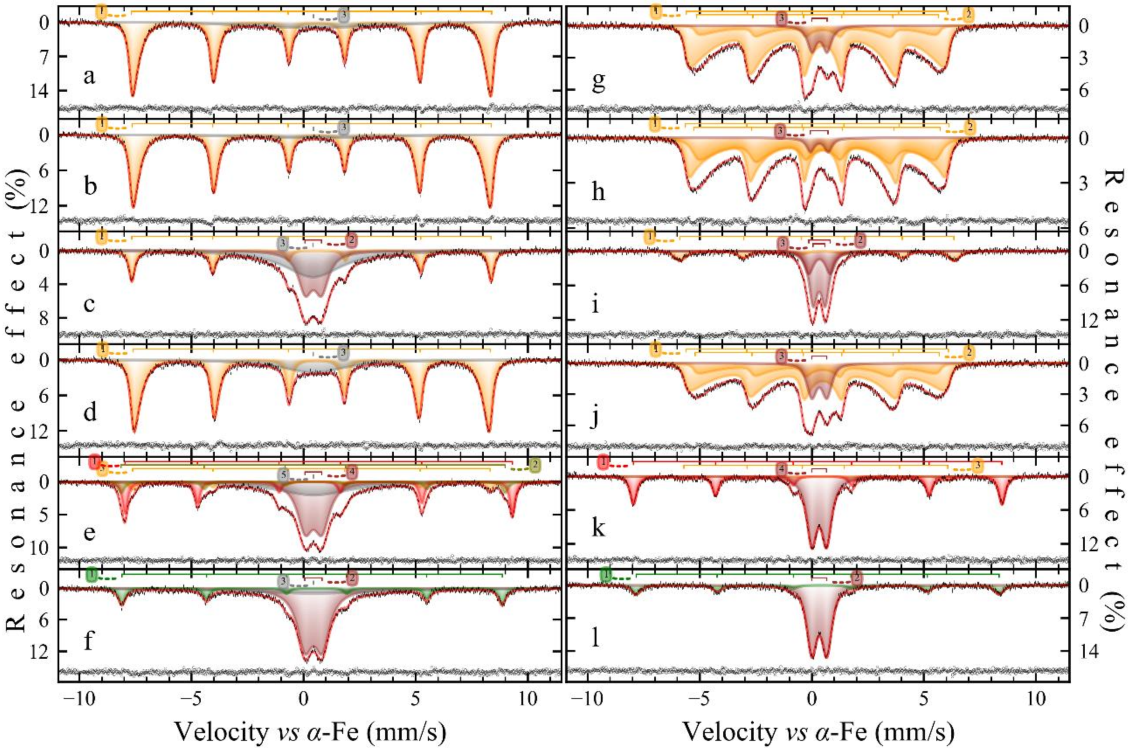

Figure 2. Mössbauer spectra of samples recorded at 78 K (*a*–*f*) and 296 K (*g*–*l*): A-N (*a, g*), A-C (*b, h*), U-N (*c, i*), U-C (*d, j*), H-N (*e, k*), and H-C (*f, l*). Subspectra are labeled in accordance with Table 3. Error bars for the experimental data points are shown; residuals obtained by subtracting the fitted model from the experimental spectra are displayed beneath each corresponding plot

The Mössbauer spectra exhibit pronounced temperature-dependent features, consistent with the known behavior of iron (oxyhydr)oxides [42–44] and nanostructured iron-containing phases [45–47]. In particular, Samples A-N, A-C, U-C, all of which were confirmed by XRD to consist primarily of goethite (79.4 %, 96.4 %, and 96 %, respectively), display sextets characteristic of magnetically ordered α-FeOOH. At 296 K (room temperature) (Fig. 2*f*, *h*), the spectra of these samples are dominated by heavily distorted sextets with broadened inner resonance lines, indicative of partial magnetic relaxation typical of nanocrystalline goethite.

Upon cooling to 78 K (liquid nitrogen temperature), these spectra evolve into more well-resolved, weakly distorted sextets with narrower lines (Fig. 2*a*, *c*), reflective of reduced thermal fluctuation and stronger magnetic ordering at low temperature. The observed behavior conforms to the many-state superparamagnetic relaxation model, [48] and the spectra were successfully fitted using two correlated relaxation sextets at 296 K and a single relaxation sextet at 78 K. The extracted hyperfine parameters align closely with literature values for goethite, [49–51] reinforcing its dominant presence in these samples. From these relaxation spectra, the ratio of magnetic anisotropy energy to thermal energy (α) was calculated using the relation:

$$\alpha = \frac{KV}{k_B T}, \tag{1}$$

where K is the magnetic anisotropy constant (assumed at 1×10^5 J m^{-3} at room temperature [52]), V is the magnetic domain volume, k_B is the Boltzmann constant, and T is the absolute temperature. Based on this model, estimated domain volumes were 114.9 nm^3 for Sample A-N and 100.5 nm^3 for Sample U-N, suggesting nanoscale magnetic domains typical of weakly interacting goethite NPs. In contrast, Samples U-N, H-N, H-C identified by XRD as mixed-phase systems, exhibited Mössbauer spectra at 296 K dominated by broad doublets superimposed on low-intensity sextets (Fig. 2*g*, *i*, *j*).

Upon cooling to 78 K (Fig. 2*b*, *d*, *e*), sextet intensity increased modestly while the doublets became broader and less distinct. These complex spectra were accurately fitted using a combination of singlets, doublets, and sextets modelled with pseudo-Voigt line shapes (Table 3). For Sample U-N, the sextet component, accounting for over 20 % of the total spectral area, was again attributed to goethite, consistent with its identification as the sole ferromagnetic phase. Sample H-N exhibited a lower goethite content (~7 %) but also revealed a distinct hematite (α-Fe_2O_3) contribution of at least 20 %, corroborated by its characteristic hyperfine field values [47, 51, 53]. In addition, at low temperature, an extra sextet emerged in Sample H-N whose parameters match those reported for ferroxyhite (δ-FeOOH), [42, 54, 55] indicating the presence of this metastable intermediate. Sample H-C presented a unique spectral profile. The dominant sextet observed at 78 K displayed hyperfine parameters that deviate from those of goethite or hematite, and were instead consistent with maghemite (γ-Fe_2O_3) [55–57]. The accompanying doublets and singlets, attributed to Fe^{3+} in octahedral coordination, are indicative of superparamagnetic or magnetically collapsed states, characteristic of nanosized ferrihydrite or disordered phases. Overall, the Mössbauer data affirm the strong influence of synthesis conditions not only on phase composition but also on magnetic domain properties, underscoring the intricate interplay between chemical environment, thermal treatment, and NPs magnetism.

Table 3

Hyperfine parameters derived from Mössbauer spectra of iron (oxyhydr)oxide samples recorded at different temperatures

Temperature, K		77.7(3)							296(3)							
Sample	№	$^*\delta$	ε {Δ=2ε}	Γ_{exp}	H_{eff}	S	α	Site/Phase	№	δ	ε {Δ=2ε}	Γ_{exp}	H_{eff}	S	α	Site/Phase
		mm s^{-1}			kOe	%				mm s^{-1}			kOe	%		
A-N	1	0.48	–0.11	0.30	498.23	83.6	16.9	α-FeOOH	1	0.37	–0.13	0.29	361.8	75.8	2.81	α-FeOOH
									2	0.38	–0.12	0.29	334.6	16.2		
	3	0.45		6.98		16.4		Fe^{3+}_{Oh}	3	0.34	{0.67}	0.483		7.95		Fe^{3+}_{Oh}
A-C	1	0.48	–0.11	0.31	496.85	87.9	17.9	α-FeOOH	1	0.37	–0.13	0.24	364.9	56	3.135	α-FeOOH
									2	0.36	–0.13	0.52	340.6	40		
	3	0.45		7.2		12.1		Fe^{3+}_{Oh}	3	0.34	{0.79}	0.42		3.72		Fe^{3+}_{Oh}
U-N	1	0.48	–0.12	0.32	496.96	21.31		α-FeOOH	1	0.37	–0.13	0.617	379.2	26.5		α-FeOOH
	2	0.44	{0.73}	0.772		32.6		Fe^{3+}_{Oh}	2	0.34	{0.96}	0.51		24		Fe^{3+}_{Oh}
	3	0.426		3.09		46.1		Fe^{3+}_{Oh}	3	0.33	{0.532}	0.452		49		Fe^{3+}_{Oh}
U-C	1	0.48	–0.11	0.31	494.54	75.1	15.74	α-FeOOH	1	0.37	–0.12	0.31	363.3	64.9	2.459	α-FeOOH
									2	0.36	–0.12	0.31	337.6	23.1		
	3	0.436		3.52		24.9		Fe^{3+}_{Oh}	3	0.33	{0.67}	0.54		12.0		Fe^{3+}_{Oh}
H-N	1	0.48	0.20	0.30	535.96	20.1		α-Fe_2O_3	1	0.37	–0.10	0.36	509.90	34.5		α-Fe_2O_3
	2	0.48	–0.05	0.354	531.0	8.1		δ-FeOOH								
	3	0.47	–0.12	0.388	494.5	6.7		α-FeOOH	3	0.35	–0.17	0.76	364.8	7.0		α-FeOOH
	4	0.44	{0.75}	0.826		37.2		Fe^{3+}_{Oh}	4	0.33	{0.66}	0.55		58.5		Fe^{3+}_{Oh}
	5	0.453		4.03		27.9		Fe^{3+}_{Oh}								
H-C	1	0.48	–0.10	0.384	526.07	16.1		γ-Fe_2O_3	1	0.37	–0.10	0.520	501.8	21.4		γ-Fe_2O_3
	2	0.44	{0.77}	0.839		57.4		Fe^{3+}_{Oh}	2	0.34	{0.67}	0.54		78.6		Fe^{3+}_{Oh}
	3	0.45		7.8		26.5		Fe^{3+}_{Oh}								

[*] δ is the isomer shift, ε (Δ=2ε) is the quadrupole shift (splitting), Γ_{exp} is the line width, H_{eff} is the hyperfine magnetic field, S is the relative area of the subspectrum, α is as (1)

Structural Evolution and Morphological Features of Synthesized NPs

The results of the XRD and Mössbauer spectroscopy data processing confirms that controlled synthesis through the dissolution–recrystallization of thermodynamically unstable ferrihydrite leads predominantly to goethite (α-FeOOH) NPs formation under suitable conditions. Ferrihydrite, a poorly crystalline iron oxide typically approximated by the formula $5Fe_2O_3{\cdot}9H_2O$, [8] is widely recognized as the first-formed phase during iron(III) hydrolysis. However, its exact stoichiometry remains debated. The physicochemical parameters governing its transformation have been thoroughly investigated by Oulego et al. [14, 16], who demonstrated that the final phase (goethite vs. hematite) is strongly dependent on pH and can proceed via either a dissolution–precipitation mechanism or solid-state transformation.

Cudennec et al. [16] provided further mechanistic insights into goethite formation by comparing the crystallographic frameworks of relevant intermediates. In our study, the role of precursor chemistry emerged as a significant factor influencing both phase composition and morphology. For instance, in Sample A-N, an additional phase, identified as a paramagnetic Fe^{3+} component, was observed alongside goethite (79.4 %), likely resulting from the slower dissociation kinetics of $Fe(NO_3)_3$ compared to $FeCl_3$. This delay in hydrolysis could favor the formation of metastable iron oxyhydroxide phases.

Temperature also exerted a profound influence on phase evolution. In hydrothermal syntheses, elevated temperatures not only accelerated hydrolysis and crystallization kinetics but also altered the redox dynamics of Fe species and facilitated active oxygen species generation, especially under ultrasonic irradiation [1]. These thermal conditions favored the formation of hematite (α-Fe_2O_3), [16] particularly in systems using the weaker base NH_4OH, which may suppress the formation of strongly basic iron hydroxides and thus shift the equilibrium toward oxide phases. Collectively, these parameters shaped not only the phase composition but also the particle morphology.

Morphological Analysis by TEM

Transmission Electron Microscopy (TEM) imaging (Fig. 3) revealed strong correlations between synthesis conditions and NPs morphology.

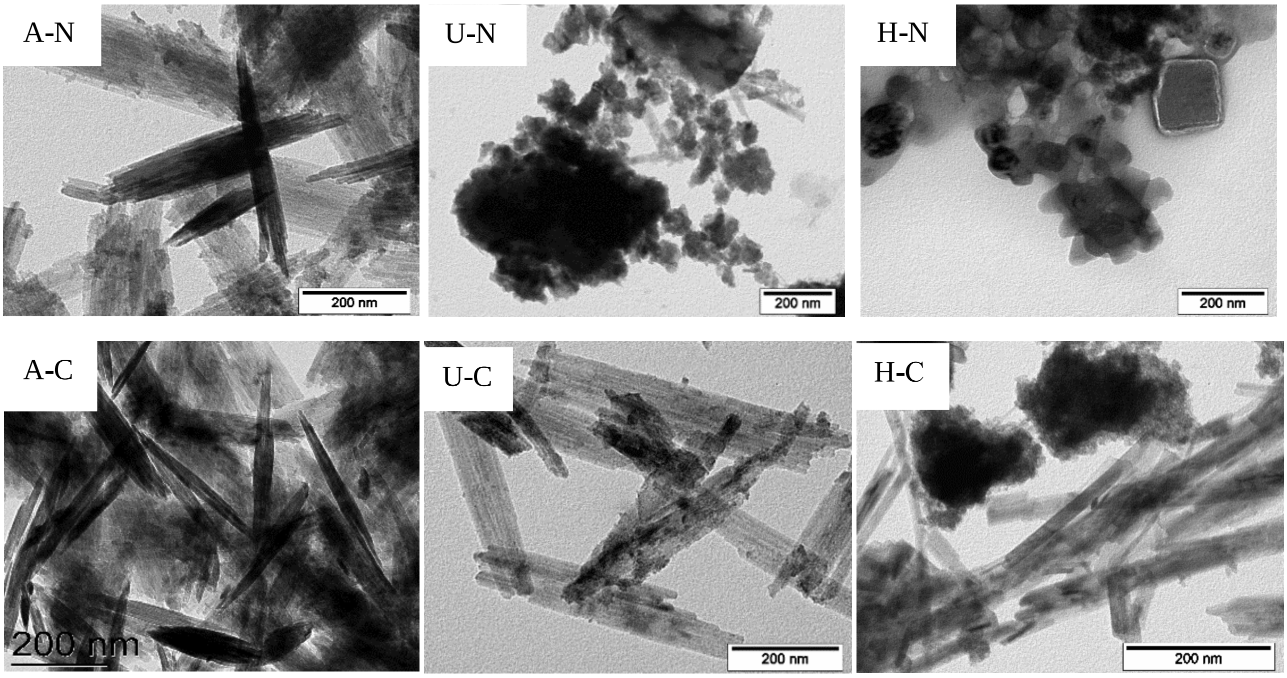

Figure 3. Transmission electron microscopy (TEM) images of iron (oxyhydr)oxide NPs samples

Samples A-N, A-C, and U-C, which were identified as predominantly goethite by XRD and Mössbauer spectroscopy, exhibited the characteristic acicular (needle-like) or rod-like morphologies typical of α-FeOOH [58–61]. These results are consistent with the observations of Martina et al. [1] (particularly for aging and hydrothermal pathways, despite our use of ferric (III) chloride hexahydrate instead of ferric (III) nitrate nonahydrate) and Hinrichs et al. [20], who also reported needle-shaped goethite NPs formed via comparable synthesis routes. Sample U-C, although morphologically similar to A-N and A-C, displayed slightly less-defined crystallinity and structural uniformity. This effect is likely attributable to the mechanical stresses induced by ultrasonic treatment, which may introduce lattice defects or disrupt ordered growth.

Interestingly, Sample H-C, despite containing only 1 % goethite according to XRD and being primarily composed of ferrihydrite (84.3 %) and hematite (14.7 %), also exhibited rod-like structures. This suggests that even minor amounts of goethite may dictate the overall particle morphology, either through templated growth or preferential aggregation within mixed-phase systems.

Sample U-N presented a markedly different appearance. As shown in Figure 3, it consists mainly of disordered aggregates resembling amorphous or nanocrystalline ferrihydrite, [38] consistent with its high ferrihydrite content (79.7 % by XRD) and the presence of broad doublets in its Mössbauer spectrum.

The morphology of Sample H-N (Fig. 3) closely resembles that of hematite, typically reported as rhombohedral or diamond-like in shape [62]. This observation correlates well with the high α-Fe_2O_3 content determined by XRD (76.7 %) and Mössbauer analysis. Previous studies [63, 64] have shown that mixed goethite–hematite systems often form agglomerates in which distinct phases are not easily differentiated, particularly at elevated synthesis temperatures (e.g., 90 °C). Similar dual-phase morphologies were reported by Combes et al. [65] and observed again by Vu et al. [66], supporting the inference that hematite dominates the particle shape in these hybrid systems.

Consistent with these findings, the morphology of Sample H-N reflects its dual composition, 7 % goethite and >20 % hematite. Despite this complexity, nanocrystalline domains with an average length of 78 ± 28 nm were readily distinguished via TEM imaging (Fig. 3), suggesting partial phase separation and crystallite coarsening within the sample.

Particle Size Distribution and Polydispersity

Although Samples A-N (79.4 % goethite), A-C (96.4 % goethite), and U-C (96 % goethite) share a predominantly goethite composition, their particle size distributions reveal notable differences influenced by synthesis conditions, particularly the application of ultrasonic treatment [67]. Sample U-C, synthesized via ultrasonic conversion, exhibited the broadest size distribution, with an average particle length of 560 ± 105 nm and width of 85 ± 24 nm. In contrast, Sample A-N yielded particles with a length of 476 ± 83 nm and width of 113 ± 27 nm, while Sample A-C produced more compact particles, averaging 389 ± 75 nm in length and 93 ± 28 nm in width (Fig. 4).

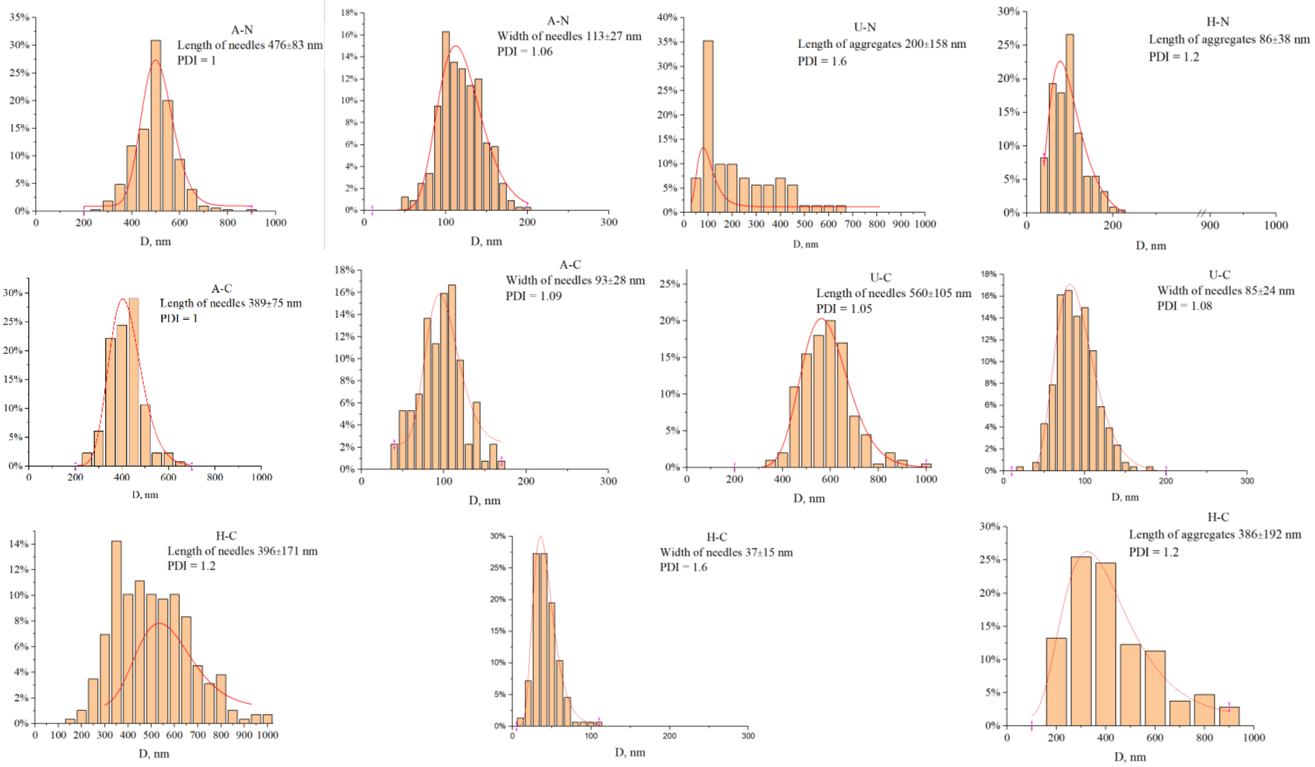

Figure 4. Particle size distribution of iron (oxyhydr)oxide NPs

The broader distribution in Sample U-C likely reflects the cavitation-driven fragmentation and nucleation associated with ultrasonic treatment, which can both promote particle refinement and introduce heterogeneity. Interestingly, Sample U-N, also prepared under ultrasonic conditions, exhibited a markedly narrower size distribution. This observation suggests that the nature of the precipitated phase plays a critical role in determining the effect of ultrasound on particle dispersion and growth kinetics. The homogeneity of particle size distribution was assessed by calculating the polydispersity index:

$$K_p = \frac{\partial}{\Delta}, \tag{2}$$

where K_p is the polydispersity index (PDI), ∂ is the weighted average particle radius (accounting for the relative abundance of each particle size), and Δ is the arithmetic mean radius. A PDI value near 1 indicates a highly monodisperse population, whereas values approaching or exceeding 2 signify broader and more heterogeneous distributions.

Considering the effect of iron salt ions (Cl^- and NO_3^-) on the polydispersity of goethite NPs, it can be assumed that the use of nitrate ions leads to the formation of monodisperse needle-shaped forms (PDI = 1.0–1.2). Chloride ions observe the aggregation of particles with PDI = 1.6. Samples A-N and A-C, obtained via low-temperature aging of ferrihydrite, exhibited PDI values of 1.0, indicating exceptional homogeneity and monodispersity.

The most uniform particle populations were still obtained under room-temperature aging conditions (Samples A-N and A-C), reinforcing the value of controlled, low-energy precipitation pathways in producing well-defined goethite nanocrystals.

Conversely, broader distributions were observed in Samples U-N (PDI = 1.6), H-N (PDI = 1.2), and H–C (PDI = 1.6), corresponding to syntheses involving elevated temperatures and/or hydrothermal treatment. These higher PDI values reflect not only greater size variability but also increased morphological and compositional heterogeneity, emphasizing the cumulative influence of precursor type, basic agent, temperature, and reaction time on NPs uniformity.

Textural Characteristics (BET/BJH Analysis)

The textural properties of the synthesized NPs were investigated using nitrogen adsorption–desorption isotherms at liquid nitrogen temperature, with results summarized in Figure 5.

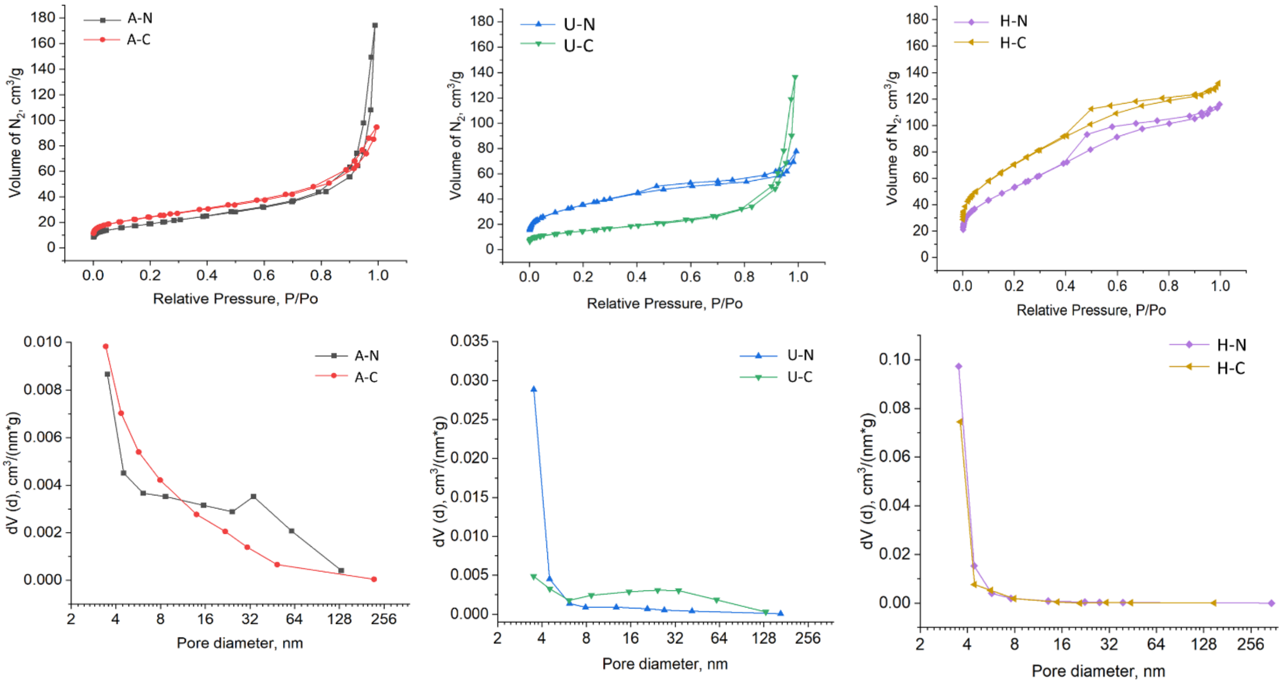

Figure 5. Low-temperature (77 K) nitrogen adsorption/desorption isotherms
and corresponding pore size distribution of iron (oxyhydr)oxide samples

According to the International Union of Pure and Applied Chemistry (IUPAC) classification, all samples exhibit Type IV isotherms, characteristic of mesoporous materials, indicating multilayer adsorption and the occurrence of capillary condensation within mesopores.

Distinct hysteresis loop types were observed across different synthesis methods, reflecting variations in pore structure. Samples A-N and U-C displayed H3-type hysteresis loops, typically associated with cavitation-controlled evaporation processes and slit-like pores formed between non-rigid aggregates of plate-like particles. In contrast, Samples U-N, H-N, and H-C demonstrated H4-type hysteresis, also indicative of slit-shaped pores but more commonly associated with narrow, micropore-like structures within porous solids.

In several samples, a pronounced uptake at low relative pressures ($P/P_0 < 0.1$) suggests the presence of micropores. Moreover, the absence of a plateau near $P/P_0 \approx 1$ implies an open pore network with interparticle voids, lacking closed porosity. The SSA values calculated using the Brunauer–Emmett–Teller (BET) method, and average pore diameters, determined via the Barrett–Joyner–Halenda (BJH) model (Table 4), further elucidate the differences among samples. The goethite-dominant samples (A-N, A-C and U-C) exhibited moderately high SSA values ranging from 53 to 88 $m^2 g^{-1}$. These values are consistent with samples demonstrating the needle-like morphology observed in TEM micrographs and are typical of well-crystallized goethite NPs with defined mesoporosity.

Table 4

Textural properties of samples

Sample	BET		BJH	
	SSA, $m^2 g^{-1}$	Pore volume, $cm^3 g^{-1}$	Pore volume, $cm^3 g^{-1}$	Pore diameter, nm
A-N	69.0	0.27	0.26	3.51
A-C	87.8	0.15	0.12	3.40
U-N	127.8	0.12	0.07	3.52
U-C	52.5	0.21	0.20	3.44
H-N	198.5	0.18	0.12	3.52
H-C	260.5	0.20	0.11	3.60

In contrast, the heterophase samples (U-N, H-N, and H-C), which contain various combinations of ferrihydrite, hematite (H-N and H-C) in addition to goethite, showed more variable SSA values. Notably, Sample H-C exhibited the highest SSA (260 $m^2 g^{-1}$) among all samples, which can be attributed to its ferrihydrite-rich composition and greater contribution of microporous features.

As reported by Chen et al. [68], while high SSA generally offers more sites, goethite with a relatively lower SSA can sometimes exhibit increased surface roughness or defects, which may enhance sorption efficiency by providing highly accessible active sites for adsorbate interaction. Conversely, high SSA values (as observed in Samples A-C, U-N, H-N, and H-C) often stem from microporous structures, which can impose diffusional constraints. The slow diffusion kinetics within narrow pores may, in certain applications, limit sorption efficiency despite the higher available SSA [69].

These findings underscore the importance of not only maximizing SSA in sorptive materials but also tailoring pore architecture and morphology to optimize accessibility and transport within the porous network.

Conclusions

This study provides a comprehensive framework for understanding the physicochemical principles that govern the controlled synthesis of biocompatible, phase-pure goethite (α-FeOOH) nanoparticles with tunable structural and morphological features. By systematically exploring multiple synthesis routes, including variations in temperature, reaction time, and ultrasonic treatment, and for the first time, precursor type (iron nitrate vs. chloride), alkalizing agent (NH_4OH vs. NaOH), we have elucidated the critical parameters that dictate nanoparticle formation pathways and final properties.

Our results highlight that the choice of iron source and alkali was found to be equally consequential: $FeCl_3$ and NaOH facilitated rapid hydrolysis and crystallization, promoting goethite formation, whereas NH_4OH, particularly under hydrothermal conditions, often led to multiphase systems involving ferrihydrite and hematite.

Regardless of iron source and alkalizing agent, temperature emerged as a dominant factor in driving crystal growth and phase transitions. Hydrothermal treatments at 90 °C resulted in markedly increased particle sizes and more complex phase compositions, underscoring the importance of kinetic control in phase-selective synthesis.

Collectively, these findings advance the rational design of iron (oxyhydr)oxide nanoparticles by providing actionable insights into how synthesis variables, namely iron and alkali source translate into structural and functional outcomes. The ability to tailor goethite nanomaterials with predictable microstructures positions them as promising candidates for a wide spectrum of applications, including biomedical scaffolds, catalysis, nanoscale sorbents. This work thus lays the groundwork for the future development of safe, functionally optimized iron-based nanomaterials with high application relevance.

Funding

The study was supported by a grant from the Russian Science Foundation (No. 24-14-20030, “Assessment of the negative impact of oil pollution on natural microbiocenoses by methods of bioassay and molecular dynamics”, https://rscf.ru/en/project/24-14-20030/).

*Author Information**

**The authors' names are presented in the following order: First Name, Middle Name and Last Name*

Sofia Magomadaevna Mulyukina (*corresponding author*) — 3rd year PhD Student, Department of Chemistry, Surgut State University, 628403, Surgut, Russia; e-mail: sbolotskaya@inbox.ru; https://orcid.org/0009-0003-9530-4241

Artur Albertovich Dzeranov — Assistant Professor, Department of Advanced Materials and Technologies for Aerospace Applications, Moscow Aviation Institute (National Research University), 125993, Moscow, Russia; Junior Research Fellow of Laboratory of Metal Polymers, Federal Research Center of Problems of Chemical Physics and Medicinal Chemistry, Russian Academy of Sciences, Semenov avenue, 1, 142432, Chernogolovka, Moscow region, Russia; e-mail: arturdzeranov99@gmail.com; https://orcid.org/0000-0003-3240-9321

Denis Alexandrovich Pankratov — PhD in Chemical Sciences, Department of Chemistry, Lomonosov Moscow State University, 119991, Moscow, Russia; Moscow Institute of Physics and Technology (National Research University), Institutskii per. 9, 141701, Dolgoprudny, Russia; e-mail: pankratov@radio.chem.msu.ru, https://orcid.org/0000-0001-6557-2753

Lyubov Sergeevna Bondarenko — PhD in Chemical Sciences, Associate Professor, Department of Advanced Materials and Technologies for Aerospace Engineering, Moscow Aviation Institute (National Research University), 125993, Moscow, Russia; e-mail: l.s.bondarenko92@gmail.com; https://orcid.org/0000-0002-3107-0648

Gulsara Damirovna Kugabaeva — 4th year PhD Student, Moscow Aviation Institute (National Research University), 125993, Moscow, Russia, Federal Research Center of Problems of Chemical Physics and Medicinal Chemistry, Russian Academy of Sciences, Moscow Region, Russia; e-mail: gulsara_kugabaev@mail.ru, https://orcid.org/0009-0006-7749-6384

Mikhail Vladimirovich Prokofiev — PhD in Chemical Sciences, Department of Advanced Materials and Technologies for Aerospace Applications, Moscow Aviation Institute (National Research University), 125993, Moscow, Russia; e-mail: mikepro1953@rambler.ru

Kamila Asylbekovna Kydralieva — Doctor of Chemical Sciences, Department of Advanced Materials and Technologies for Aerospace Applications, Moscow Aviation Institute (National Research University), 125993, Moscow, Russia; e-mail: kamila.kydralieva@gmail.com; https://orcid.org/0000-0002-4596-4140

Author Contributions

The manuscript was written through contributions of all authors. All authors have given approval to the final version of the manuscript. CRediT: **Sofia Magomadaevna Mulyukina** investigation, Software; **Artur Albertovich Dzeranov** investigation, writing, editing; **Denis Alexandrovich Pankratov** investigation, writing; **Lyubov Sergeevna Bondarenko** writing, Software; **Gulsara Damirovna Kugabaeva** investigation;

Mikhail Vladimirovich Prokofiev investigation; **Kamila Asylbekovna Kydralieva** conceptualization, data curation, methodology, writing — reviewing and editing.

Acknowledgments

The Mössbauer spectroscopy analysis was conducted as part of the state assignment of *Lomonosov Moscow State University*, “Solving problems of nuclear energy and environmental safety, as well as diagnostics of materials using ionizing radiation” (No. 122030200324-1). Low-temperature nitrogen adsorption measurements were performed in accordance with the state research assignments registered under No. 124013000757-0. These experiments were carried out using the facilities of *the Multi-User Analytical Center of the Federal Research Center of Problems of Chemical Physics and Medicinal Chemistry of the Russian Academy of Sciences*.

Declaration of Generative AI and AI-Assisted Technologies in the Writing Process

During the preparation of this work, the authors used grammar-checking tools (Grammarly and equivalent standard proofreading instruments) only to refine the language of the manuscript. After using these tools, the authors thoroughly reviewed and edited the text as needed and take full responsibility for the content of the publication.

Conflicts of Interest

The authors declare no conflict of interest.

References

1 Martina, M. R., Zoli, L., Sani, E. (2022). Synthesis and characterization of goethite (α-FeOOH) magnetic nanofluids. *International Journal of Thermofluids*, *15*, 100169. https://doi.org/10.1016/j.ijft.2022.100169

2 Kubiak, A., Voronkina, A., & Jesionowski, T. (2023). Creation of a 3D Goethite–Spongin Composite Using an Extreme Biomimetics Approach. *Biomimetics*, *8*, 533. https://doi.org/10.3390/biomimetics8070533

3 Nowacki, K., Kubiak, A., & Jesionowski, T. (2024). 3D Spongin Scaffolds as Templates for Electro-Assisted Deposition of Selected Iron Oxides. *Biomimetics*, *9*, 387. https://doi.org/10.3390/biomimetics9070387

4 Shi, Z., Zachara, J.M., & Fredrickson, J.K. (2012). Redox Reactions of Reduced Flavin Mononucleotide (FMN), Riboflavin (RBF), and Anthraquinone-2,6-disulfonate (AQDS) with Ferrihydrite and Lepidocrocite. *Environmental Science & Technology*, *46* (21), 11644–11652. https://doi.org/10.1021/es301544b

5 Zhourui, L., Manisha, M., Yichao, W., Qiaoyun, H., Peng C. (2021). Increased particle size of goethite enhances the antibacterial effect on human pathogen Escherichia coli O157:H7: A Raman spectroscopic study. Journal of Hazardous Materials, 405, 124174. https://doi.org/10.1016/j.jhazmat.2020.124174

6 Kosei, I., Eiji, A., Oluyomi, S. A. & (2024). Goethite and Hematite Nanoparticles Show Promising Anti-Toxoplasma Properties. *Pharmaceutics, 16* (3), 413. https://doi.org/10.3390/pharmaceutics16030413

7 Dulnee, S., Scheinost, A.C. (2014). Surface Reaction of SnII on Goethite (α-FeOOH): Surface Complexation, Redox Reaction, Reductive Dissolution, and Phase Transformation. *Environmental Science & Technology, 48* (16), 9341–9348. https://doi.org/10.1021/es501923z

8 Lin, Y.L., Wei, Y., Sun, Y.H. (2012). Room-temperature synthesis and photocatalytic properties of lepidocrocite by monowavelength visible light irradiation. *Journal of Molecular Catalysis A: Chemical, 353–354,* 67–73. https://doi.org/10.1016/j.molcata.2011.11.006

9 Tiar, K., Soualah, A., Bisio, C., Guidotti, M. (2024). Effect of initial solution pH on 4-nitrophenol oxidation through homogeneous/heterogeneous photo-Fenton process using goethite/H_2O_2 system. *Journal of Photochemistry and Photobiology A: Chemistry*, *447*, 115184. https://doi.org/10.1016/j.jphotochem.2023.115184

10 Li, X., Niu, A., Yang, S. (2024). The reduction of nitrobenzene by Fe(II)-goethite-hematite heterogeneous systems: Insight from thermodynamic parameters of reduction potential. *Journal of Environmental Management, 370*, 122404. https://doi.org/10.1016/j.jenvman.2024.122404

11 Liu, G., Yu, H., Zhou, T. (2022). Activation of peroxydisulfate by biogenic nanocomposites of reduced graphene oxide and goethite for non-radical selective oxidation of organic contaminants: Production of singlet oxygen and direct electron transfer. *Chemical Engineering Journal*, *430*, 133177. https://doi.org/10.1016/j.cej.2021.133177

12 Montes-Hernandez, G., Beck, P., & Findling, N. (2011). Fast precipitation of acicular goethite from ferric hydroxide gel under moderate temperature (30 and 70 C degrees). *Crystal Growth & Design*, *11* (6), 112264–2272. https://doi.org/10.1021/cg1016802

13 Gilbert, F., Refait, P., C., & Conforto, E. (2008). Synthesis of goethite from $Fe(OH)_2$ precipitates: Influence of Fe(II) concentration and stirring speed. *Journal of Physics and Chemistry of Solids*, *69* (8), 2124-2130. https://doi.org/10.1016/j.jpcs.2008.03.010

14 Oulego, P., Villa-García, M.A., Lacaa, A., Diaz, M. (2016). Effect of the synthetic route on the structural, textural, morphological and catalytic properties of Iron (III) oxides and oxyhydroxides. *Dalton Transactions*, 45, 9446–9459. 10.1039/C6DT00247A

15 Kuncser, A.C., Vlaicu, I.D., Pavel, O.D., Olar, R. (2021). Soft synthesis and characterization of goethite-based nanocomposites as promising cyclooctene oxidation catalysts. *RSC Advances*, *11*, 27589-27602. https://doi.org/10.1039/D1RA04211D

16 Cudennec, Y., Lecerf, A. (2006). The transformation of ferrihydrite into goethite or hematite, revisited. *Journal of Solid State Chemistry*, *179* (3), 716–722. https://doi.org/10.1016/j.jssc.2005.11.030

17 Alves, C.A.P., Palharim, P.H., & Ramos, B. (2025). Photocatalytic ammonia synthesis from nitrogen in water using iron oxides: Comparative efficiency of goethite, magnetite, and hematite. *Journal of Photochemistry and Photobiology A: Chemistry*, *460*, 116159. https://doi.org/10.1016/j.jphotochem.2024.116159

18 Adeoye A. O., Quadri, R. O., Lawal, O. S. (2023). Wet synthesis, characterization of goethite nanoparticles and its application in catalytic pyrolysis of palm kernel shell in TGA. *Results in Surfaces and Interfaces*, *11*, 100118. https://doi.org/10.1016/j.rsurfi.2023.100118

19 Kosmulski, M., Maczka, E., Jartych, E., Rosenholm, J. B. (2003). Synthesis and characterization of goethite and goethite–hematite composite: experimental study and literature survey. *Advances in Colloid and Interface Science*, *103* (1), 57–76. https://doi.org/10.1016/S0001-8686(02)00083-0

20 Hinrichs, S., Grossmann, L., & Hankiewicz, B. (2020). Goethite Nanorods: Synthesis and Investigation of the Size Effect on Their Orientation within a Magnetic Field by SAXS. *Nanomaterials*, *10* (12), 2526. https://doi.org/10.3390/nano10122526

21 Mohapatra M., Gupta S., & Mishra B.K. (2010). pH and temperature dependent facile precipitation of nano-goethite particles in $Fe(NO_3)_3$–NaOH–$NH_3NH_2HSO_4$–H_2O medium. *Colloids and Surfaces A: Physicochemical and Engineering Aspects*, 355 (1-3), 53–60. https://doi.org/10.1016/j.colsurfa.2009.11.029

22 Meret, A., Ralf, K., & Ruben, K. (2019). Electrochemical Analysis of Changes in Iron Oxide Reducibility during Abiotic Ferrihydrite Transformation into Goethite and Magnetite. *Environmental Science & Technology*, *53* (7), 3568–3578. https://doi.org/10.1021/acs.est.8b07190

23 Ristić, M., Opačak, I., & Musić, S. (2013). The synthesis and microstructure of goethite particles precipitated in highly alkaline media. Journal of Alloys and Compounds, 559, 49–56. https://doi.org/10.1016/j.jallcom.2013.01.027

24 Xu, Y., Wang, H., Ye, S., et al. (2024). Goethite adaptation prompts alterations in antibiotic susceptibility and suppresses development of antibiotic resistance in bacteria. *Science of The Total Environment*, *916*, 170248. https://doi.org/10.1016/j.scitotenv.2024.170248

25 Agresti, F., Isopi, J., Scattareggia Marchese, S., et al. (2025). Electrorheology of urea-functionalized lathlike goethite particles in silicone oil. *Colloids and Surfaces A: Physicochemical and Engineering Aspects*, *704*, 135509. https://doi.org/10.1016/j.colsurfa.2024.135509

26 Darabian, L. M., Gonçalves, G. R., Schettino, M. A., Passamani, E. C., & Freitas, J. C. C. (2022). Synthesis of nanostructured iron oxides and study of the thermal crystallization process using DSC and in situ XRD experiments. Materials Chemistry and Physics, 285, 126065. https://doi.org/10.1016/j.matchemphys.2022.126065

27 Zhang, Y-X., Jia, Y. (2014). A facile solution approach for the synthesis of akaganéite (β-FeOOH) nanorods and their ion-exchange mechanism toward As (V) ions. *Applied Surface Science*, *290*, 102-106. https://doi.org/10.1016/j.apsusc.2013.11.007

28 Jia, Y., Luo, T., & Huang, X.J. (2013). Facile one-pot synthesis of lepidocrocite (γ-FeOOH) nanoflakes for water treatment. *New Journal of Chemistry*, *37* (8), 2551–2556. doi: http://dx.doi.org/10.1039/c3nj00509g

29 Fang F., Jia Y., Wu P-Y., & Peng D-Y. (2015). Facile one-pot preparation of goethite/parabutlerite nanocomposites and their removal properties and mechanism toward As(V) ions. *Applied Surface Science Journal*, *324*, 355–362. https://doi.org/10.1016/j.apsusc.2014.10.174

30 Ma, J., Zhang, X., He, Y., et al. (2015). Non-superparamagnetic iron-oxide architectures with controlled T_2 contrast ability in magnetic resonance imaging. *Applied Physics Letters*, *107*, 073701. https://doi.org/10.1063/1.4928914

31 Kang, S., Kim, G., Cheon, J. (2025). Corrugated-Surface Goethite Nanoparticles with Reduced Magnetization and Increased Surface Area for Enhanced T_1 MRI Contrast Effect. *ACS Applied Materials & Interfaces*, *17*(49), 66450–66459. https://doi.org/10.1021/acsami.5c18713

32 Serup, J., Alsing, K.K., Olsen, O., et al. (2023). On the mechanism of painful burn sensation in tattoos on magnetic resonance imaging (MRI). Magnetic substances in tattoo inks used for permanent makeup (PMU) identified: Magnetite, goethite, and hematite. *Skin Research and Technology*, *29*(3), e13281. https://doi.org/10.1111/srt.13281

33 Gulzar, A., Ayoub, N., Mir, J.F., et al. (2022). In vitro and in vivo MRI imaging and photothermal therapeutic properties of Hematite (α-Fe2O3) Nanorods. *Journal of Materials Science: Materials in Medicine*, *33* (10). https://doi.org/10.1007/s10856-021-06636-1

34 Lunin, A.V., Kolychev, E.L., & Nikitin, M.P. (2019). Synthesis of highly-specific stable nanocrystalline goethite-like hydrous ferric oxide nanoparticles for biomedical applications by simple precipitation method. *Journal of Colloid and Interface Science*, *541*, 143–149. https://doi.org/10.1016/j.jcis.2019.01.065

35 Balzar, D., Audebrand, N., Daymond, M. R., Toby, B. H. (2004). Size-strain line-broadening analysis of ceria round-robin sample. *Journal of Applied Crystallography*, *37*, 911–924. https://doi.org/10.1107/S0021889804022551

36 Nikolaeva, O.V., Terekhov, V.A. (2017). Improvement of laboratory phytotest for the ecological evaluation of soils. *Eurasian Soil Science*, *50*, 1105-1114. 10.1134/S1064229317090058

37 Skalny, M., Rokowska, A., & Bajda, T. (2024). Nanoscale surface defects of goethite governing DNA adsorption process and formation of the Goethite-DNA conjugates, *Chemosphere*, *362*, 142602. https://doi.org/10.1016/j.chemosphere.2024.142602

38 Gomez, M.A., Jiang, R., & Jia, Y. (2020). Further insights into the Fe(II) reduction of 2-line ferrihydrite: a semi in situ and in situ TEM study. *Nanoscale Advances*, *2*, 4938-4950. https://doi.org/10.1039/d0na00643b

39 Smith, S.J., Page, K., & Woodfield, B.F. (2012). Novel synthesis and structural analysis of ferrihydrite. *Inorganic Chemistry*, *51* (11), 6421–6424. https://doi.org/10.1021/ic300937f

40 Su, R., Li, C., & Lan, S. (2024). Catalytic oxidation of Mn(II) on ferrihydrite and goethite surfaces and the subsequent oxidation and immobilization of coexisting Cr(III). *Applied Geochemistry*, *175*, 106195. https://doi.org/10.1016/j.apgeochem.2024.106195

41 Okada, S., Takagi, K., Ozaki, K. (2016). Synthesis of submicron-sized acicular goethite and platelet-like hematite particles and dependence of magnetic properties of α-Fe particles on their shape and size. *Materials Chemistry and Physics*, *171*, 171–177. https://doi.org/10.1016/j.matchemphys.2016.01.002

42 Polyakov, A.Y., Sorkina, T.A., & Goodilin, E.A. (2013). Mössbauer spectroscopy of frozen solutions as a stepwise control tool in preparation of biocompatible humic-stabilized feroxyhyte nanoparticles. *Hyperfine Interactions*, *219*, 113–120. https://doi.org/10.1007/s10751-013-0812-y

43 Pankratov, D.A., Dolzhenko, V.D., & Severin, A.V. (2017). Properties of iron-containing nanohydroxyapatite-based composites. *Inorganic Materials*, *53* (1), 115–124. https://doi.org/10.1134/S0020168517010125

44 Kulikova N.A., Polyakov A.Y., & Perminova I.V. (2017). Key roles of size and crystallinity of nanosized iron hydr (oxides) stabilized by humic substances in iron bioavailability to plants. *Journal of Agricultural and Food Chemistry*, *65* (51), 11157–11169. https://doi.org/10.1021/acs.jafc.7b03955

45 Yurkov, G.Y., Shashkeev, K.A., & Koksharov, Y.A. (2016). Synthesis and magnetic properties of cobalt ferrite nanoparticles in polycarbosilane ceramic matrix. Journal of Alloys and Compounds, *686*, 421–430. https://doi.org/10.1016/j.jallcom.2016.06.025

46 Pankratov, D.A., Anuchina, M.M., Spiridonov, F.M., Krivtsov, G.G. (2020). $Fe_{3-\delta}O_4$ Nanoparticles Synthesized in the Presence of Natural Polyelectrolytes. *Crystallography Reports*, *65* (3), 393–397. https://doi.org/10.1134/S1063774520030244

47 Chernavskiy, P.A., Novakova, A.A., & Petrovskaya, G.A. (2023). Synthesis and Characterization of Hematite, Magnetite and Maghemite Supported on Silica Gel. *Magnetochemistry*, *9* (11), 228. https://doi.org/10.3390/magnetochemistry9110228

48 Jones, D.H., Srivastava, K.K.P. (1986). Many-state relaxation model for the Mössbauer spectra of superparamagnets. *Physical Review B*, *34* (11), 7542–7548. https://doi.org/10.1103/PhysRevB.34.7542

49 Zharkynbaeva, R., Dzeranov, A., & Kydralieva, K. (2024). Exploring the synergistic effects of goethite intercalated coal in the presence of humic acids for enhanced growth of Sinapis alba. *Chemical and Biological Technologies in Agriculture*, *14*, 1354. https://doi.org/10.1186/s40538-023-00530-4

50 Pankratov, D.A., Dovletyarova, E.A., & Neaman, A. (2024). Deciphering the corrosion puzzle: Nano-iron-biochar composite — Not a quick fix for metal immobilization in peat soils. *Applied Geochemistry*, *166*, 105982. https://doi.org/10.1016/j.apgeochem.2024.105982

51 Shoppert, A., Valeev, D., & Pankratov, D. (2022). High-Iron Bauxite Residue (Red Mud) Valorization Using Hydrochemical Conversion of Goethite to Magnetite. *Materials*, *15* (23), 8423. https://doi.org/10.3390/ma15238423

52 Brok, E., Frandsen, C., & Berhe, A. A. (2014). Magnetic properties of ultra-small goethite nanoparticles. *Journal of Applied Physics D: Applied Physics*, *47* (36), 365003. 10.1088/0022-3727/47/36/365003

53 Shoppert, A., Valeev, D., Loginova, I., Pankratov, D. (2023). Low-Temperature Treatment of Boehmitic Bauxite Using the Bayer Reductive Method with the Formation of High-Iron Magnetite Concentrate. *Materials*, *16* (13), 4678. https://doi.org/10.3390/ma16134678

54 Polyakov, A.Y., Goldt, A.E., & Tretyakov, Y.D. (2012). Constrained growth of anisotropic magnetic δ-FeOOH nanoparticles in the presence of humic substances. *CrystEngComm*, *14* (23), 8097. https://doi.org/10.1039/C2CE25886B

55 Dzeranov, A., Bondarenko, L., & Kydralieva, K. (2023). Iron Oxides Nanoparticles as Components of Ferroptosis-Inducing Systems: Screening of Potential Candidates. *Magnetochemistry*, *9* (1), 3. https://doi.org/10.3390/magnetochemistry9010003

56 Rostovshchikova, T.N., Korobov, M.S., & Gubin, S.P. (2005). Catalytic conversions of chloroolefins over iron oxide nanoparticles 2. Isomerization of dichlorobutenes over iron oxide nanoparticles stabilized on the surface of ultradispersed poly(tetrafluoroethylene). *Russian Chemical Bulletin*, *54* (6), 1425–1432. https://doi.org/10.1007/s11172-005-0422-1

57 Klygach, D.S., Vakhitov, M.G., & Trukhanov, A.V. (2021). MCC: Specific of preparation, correlation of the phase composition and electrodynamic properties. Journal of Magnetism and Magnetic Materials. *526*, 167694. https://doi.org/10.1016/j.jmmm.2020.167694

58 Campo, B.C., Rosseler, O., & Volp M.A. (2008). On the nature of goethite, Mn-goethite and Co-goethite as supports for gold nanoparticles Mater. *Materials Chemistry and Physics*, *109*, 448-454. https://doi.org/10.1016/j.matchemphys.2007.12.014

59 Tartaj, P., Amarilla, J.M. (2011). Iron oxide porous nanorods with different textural properties and surface composition: Preparation, characterization and electrochemical lithium storage capabilities. *Journal of Power Sources*, *196* (4), 2164–2170. https://doi.org/10.1016/j.jpowsour.2010.09.116

60 Maiti, D., Aravindan, V., Madhavi, S., Sujatha, P. D. (2015). Electrochemical performance of hematite nanoparticles derived from spherical maghemite and elongated goethite particles. *Journal of Power Sources*, *276*, 291–298. https://doi.org/10.1016/j.jpowsour.2014.11.097

61 Harris, R.A. (2024). Phase transformation of magnetite and goethite nanoparticles controlled by pH: Experimental and simulation study of cuboid magnetic nanoparticles prepared with NaOH. *Solid State Sciences*, *148*, 107416. https://doi.org/10.1016/j.solidstatesciences.2023.107416

62 Zhu, M., Wang, Y., Meng, D., Qin, X., Diao G. (2012). Hydrothermal Synthesis of Hematite Nanoparticles and Their Electrochemical Properties. *The Journal of Physical Chemistry C*, *116* (30), 16276–16285. https://doi.org/10.1021/jp304041m

63 Chen, S.A., Heaney, P.J., & Stubbs, J.E. (2022). Hematite-goethite ratios at pH 2–13 and 25–170 °C: A time-resolved synchrotron X-ray diffraction study. *Chemical Geology*, *606*, 120995. https://doi.org/10.1016/j.chemgeo.2022.120995

64 Akinwekomi, V., Maree, J.P., & Chatzisymeon, E. (2020). Beneficiation of acid mine drainage (AMD): A viable option for the synthesis of goethite, hematite, magnetite, and gypsum — Gearing towards a circular economy concept. *Minerals Engineering*, *148*, 106204. https://doi.org/10.1016/j.mineng.2020.106204

65 Combes, J.M., Manceau, A., Calas, G. (1990). Formation of ferric oxides from aqueous solutions: A polyhedral approach by X-ray Absorption Spectroscopy: II. Hematite formation from ferric gels. *Geochimica et Cosmochimica Acta*, *54*, 1083–1091. https://doi.org/10.1016/0016-7037(90)90440-V

66 Vu, H.P., Shaw, S., Brinza, L., Benning, L.G. (2013). Partitioning of Pb(II) during goethite and hematite crystallization: Implications for Pb transport in natural systems. *Applied Geochemistry*, *39*, 119-128. https://doi.org/10.1016/j.apgeochem.2013.10.001

67 De La Vega, J.C., Elischer, P., Schneider, T., Häfeli, U.O. (2013). Uniform polymer microspheres: monodispersity criteria, methods of formation and applications. *Nanomedicine*, *8*, 265–285. https://doi.org/10.2217/nnm.12.210

68 Chen, K., Guo, C., & Dang Z. (2024). Using machine learning to explore oxyanion adsorption ability of goethite with different specific surface area. *Environmental Pollution*, *343*, 123162. https://doi.org/10.1016/j.envpol.2023.123162

69 Belloni, C., Korving, L., & Dugulan, A.I. (2024). Zn induced surface modification of stable goethite nanoparticles for improved regenerative phosphate adsorption. *Colloids and Surfaces A: Physicochemical and Engineering Aspects*, *687*, 133476. https://doi.org/10.1016/j.colsurfa.2024.133476